












RESEARCH ARTICLE | AUGUST 11 2020

## An integrated ultra-high vacuum apparatus for growth and *in situ* characterization of complex materials

G. Vinai ; F. Motti ; A. Yu. Petrov; V. Polewczyk ; V. Bonanni ; R. Edla ; B. Gobaut ; J. Fujii ; F. Suran; D. Benedetti; F. Salvador; A. Fondacaro; G. Rossi ; G. Panaccione ; B. A. Davidson ; P. Torelli 



Rev. Sci. Instrum. 91, 085109 (2020)

<https://doi.org/10.1063/5.0005302>



### Articles You May Be Interested In

Structural and electronic properties of the pure and stable elemental 3D topological Dirac semimetal  $\alpha$ -Sn

*APL Mater.* (March 2020)

Polycrystalline metal surfaces studied by X-ray photoelectron spectro-microscopy

*AIP Conference Proceedings* (May 2000)

Tuning the period of elastic MnAs/GaAs(001)  $\alpha - \beta$  pattern by Fe deposition

*Appl. Phys. Lett.* (December 2010)



Optimize  
Your  
Research

Our Vacuum Gauges Provide  
More Process Control  
and Operational Reliability



# An integrated ultra-high vacuum apparatus for growth and *in situ* characterization of complex materials

Cite as: Rev. Sci. Instrum. 91, 085109 (2020); doi: 10.1063/5.0005302

Submitted: 19 February 2020 • Accepted: 29 July 2020 •

Published Online: 11 August 2020



View Online



Export Citation



CrossMark

G. Vinai,<sup>1,a)</sup> F. Motti,<sup>1,2</sup> A. Yu. Petrov,<sup>1</sup> V. Polewczyk,<sup>1</sup> V. Bonanni,<sup>1,2</sup> R. Edla,<sup>1</sup> B. Gobaut,<sup>3</sup> J. Fujii,<sup>1</sup> F. Suran,<sup>1</sup> D. Benedetti,<sup>1</sup> F. Salvador,<sup>1</sup> A. Fondacaro,<sup>1</sup> G. Rossi,<sup>1,2</sup> G. Panaccione,<sup>1</sup> B. A. Davidson,<sup>1,4</sup> and P. Torelli<sup>1</sup>

## AFFILIATIONS

<sup>1</sup>Istituto Officina dei Materiali (IOM)-CNR, Laboratorio TASC, Area Science Park, S.S. 14 Km 163.5, Trieste I-34149, Italy

<sup>2</sup>Department of Physics, Università degli Studi di Milano, Via Celoria 16, I-20133 Milano, Italy

<sup>3</sup>Elettra-Sincrotrone Trieste S.C.p.A, Area Science Park, 34149 Basovizza, Trieste, Italy

<sup>4</sup>Stewart Blusson Quantum Matter Institute, University of British Columbia, Vancouver, British Columbia V6T 1Z4, Canada

<sup>a)</sup> Author to whom correspondence should be addressed: [vinai@iom.cnr.it](mailto:vinai@iom.cnr.it)

## ABSTRACT

Here, we present an integrated ultra-high vacuum apparatus—named MBE-Cluster—dedicated to the growth and *in situ* structural, spectroscopic, and magnetic characterization of complex materials. Molecular Beam Epitaxy (MBE) growth of metal oxides, e.g., manganites, and deposition of the patterned metallic layers can be fabricated and *in situ* characterized by reflection high-energy electron diffraction, low-energy electron diffraction, Auger electron spectroscopy, x-ray photoemission spectroscopy, and azimuthal longitudinal magneto-optic Kerr effect. The temperature can be controlled in the range from 5 K to 580 K, with the possibility of application of magnetic fields  $\mathbf{H}$  up to  $\pm 7$  kOe and electric fields  $\mathbf{E}$  for voltages up to  $\pm 500$  V. The MBE-Cluster operates for in-house research as well as user facility in combination with the APE beamlines at Sincrotrone-Trieste and the high harmonic generator facility for time-resolved spectroscopy.

© 2020 Author(s). All article content, except where otherwise noted, is licensed under a Creative Commons Attribution (CC BY) license (<http://creativecommons.org/licenses/by/4.0/>). <https://doi.org/10.1063/5.0005302>

## I. INTRODUCTION

Molecular beam epitaxy (MBE) in ultra-high vacuum (UHV) provides unique flexibility and control properties for growing complex metal oxides.<sup>1,2</sup> The quasi-equilibrium deposition conditions during the growth allow maximum control of thickness and surface termination of single-crystal epitaxial films, making it the method of choice when the low-energy properties of the grown heterostructures need to be investigated, such as charge transfer at the interface or the effects of controlled strain.<sup>3–5</sup> More generally, magnetism, ferroelectricity, and their interplay can be exploited for spintronic systems involving oxides,<sup>6</sup> multiferroics,<sup>7,8</sup> magnetoelectric heterostructures,<sup>9,10</sup> or antiferromagnetic materials.<sup>11,12</sup>

Here, we present the features and performances of the dedicated UHV MBE-Cluster system that has been optimized for our

research program on multiferroic heterostructures.<sup>13–16</sup> The apparatus is composed of a series of interconnected UHV chambers that allows the MBE growth of oxides and metallic layers and the characterization of their magnetic, chemical, surface structural, and electronic properties. High-quality, engineered samples can be grown and transferred via the UHV shuttle load lock to the neighboring APE-HE and APE-LE synchrotron beamlines,<sup>17</sup> where they can be characterized with x-ray absorption spectroscopy (XAS)/x-ray magnetic circular dichroism (XMCD) and spin-angle-resolved photoemission spectroscopy (spin-ARPES) measurements, respectively,<sup>18</sup> or to the NFFA-SPRINT laboratory<sup>19,20</sup>—a laser—high harmonic generator (HHG) source beamline for time-resolved spectroscopy and magnetometry located in the experimental hall of the FERMI Free Electron Laser at Trieste. Finally, the MBE-Cluster allows short and long distance sample transfer to remote

laboratories via the UHV shuttle and is fully compatible with a clean, atmospheric-pressure inert-gas glovebox. These combined features, rarely found among worldwide laboratories,<sup>21</sup> together with the innovative homemade design of its components, make this apparatus an extremely versatile tool for the deposition and characterization of complex heterostructures and multiferroic systems, with potential investigation of magnetoelectric logic units, a promising beyond-CMOS technology.<sup>8</sup>

The MBE-Cluster is part of the NFFA-Trieste infrastructure,<sup>22</sup> a multitechnique facility for nanoscience studies that allows the access to experiments involving the techniques described in this article via peer-reviewed proposals, which is part of the European NFFA Research Infrastructure program,<sup>23</sup> an international platform involving European laboratories and large-scale facilities. As such, the MBE-Cluster is used both for in-house research and as user facility.

## II. SYSTEM OVERVIEW

Figure 1 shows the suite of UHV apparatuses that form the MBE-Cluster. Three main chambers are interconnected by two home-built UHV bi-directional linear transfer and storage systems. The central chamber (in green), named MASK, is devoted to the e-beam deposition of metallic layers and to *in situ* surface characterization by Low-Energy Electron Diffraction (LEED), Auger Electron Spectroscopy (AES), and magneto-optic Kerr effect (MOKE) measurements at variable temperatures and applied magnetic fields up to  $\pm 7$  kOe. The bi-directional transfer systems (in orange) move the samples to the peripheral OxMBE (OxMBE) chamber (in red) or to the x-ray photoemission spectrometer (in blue), described as a previous implementation for VOLume PhotoEmission spectroscopy (VOLPE),<sup>24–26</sup> currently operating with a dedicated Al/Mg twin anode x-ray source.

The samples are mounted on four-face sample holders for *in situ* manipulation by means of UHV wobblesticks (Ferrovac WM40). The sample holders are made of solid molybdenum, titanium, or copper, either as single block versions or as split versions,

where a ceramic or sapphire gap allows for electrical insulation from ground as well as sample polarization and current flow through the sample. Samples of up to  $10 \times 5$  mm lateral dimensions and 0.1 mm–3 mm thickness<sup>14</sup> can be hosted. Docking positions for the UHV shuttle (Ferrovac VSN40S) are available along the cluster for transferring samples to other UHV apparatuses, at pressures never exceeding  $1 \times 10^{-9}$  mbar, or to the inert-gas glovebox.

### A. MASK chamber: The metal-MBE deposition and *in situ* MOKE apparatus

The MASK multifunctional UHV chamber features e-beam deposition sources for metals and *in situ* magnetization and magnetic azimuthal anisotropy analysis by means of MOKE in a single block machined expansion of the UHV chamber that fits in the gap of a laboratory electromagnet. The UHV is obtained by turbomolecular pumping (240 l/s) with oil-free scroll pump backing. The UHV sample manipulator has the main travel horizontal and can rotate around its axis, via two Sim-Stepper motors acting on a differentially pumped UHV feedthrough, with a joystick remote control. The sample positioning is accurate and reproducible with a micrometric resolution for the horizontal translation and with a  $0.05^\circ$  resolution for the rotation.<sup>19</sup> The two linear perpendicular axes are controlled manually by two translators with similar accuracy.

The chamber presents seven C40 ports in the lower part that allow installing electron beam evaporation sources (Ferrovac EV40FC evaporators) for metals at different angles with respect to the vertical ( $0^\circ$ ,  $15^\circ$ ,  $30^\circ$ , or  $60^\circ$ ). A retractable quartz crystal microbalance (QCM) (Inficon STM-2) is used to calibrate the deposition rate of the evaporator sources before and after deposition on the substrate. The system allows for installation of valved retractable evaporator sources, with a dedicated UHV pumping system. In this way, it is possible to substitute the evaporator unit without venting the whole chamber, with local pumping and bake-out procedure, for a quick replacement of materials or maintenance. The MASK chamber also includes *in situ* calibrated gas inlets, ion sputtering (SPECS IQE-11 A), a LEED, and an electron spectrometer in a four-grid setup AES (OCI BDL800).

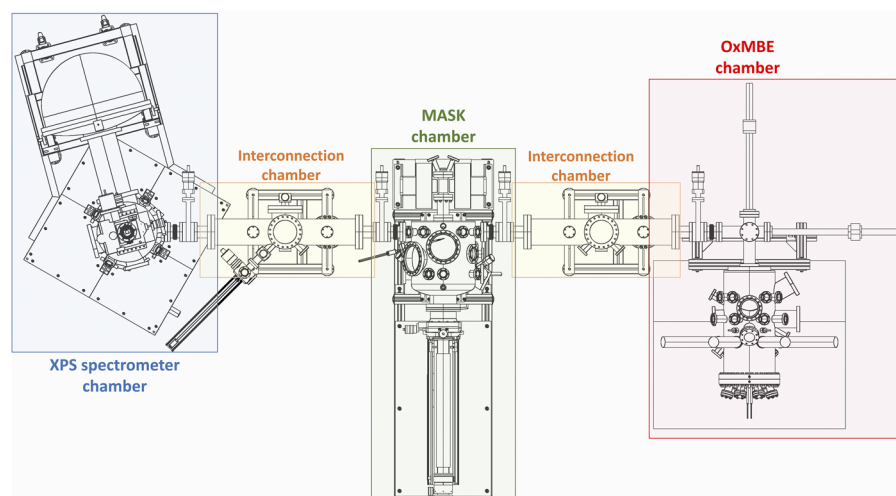
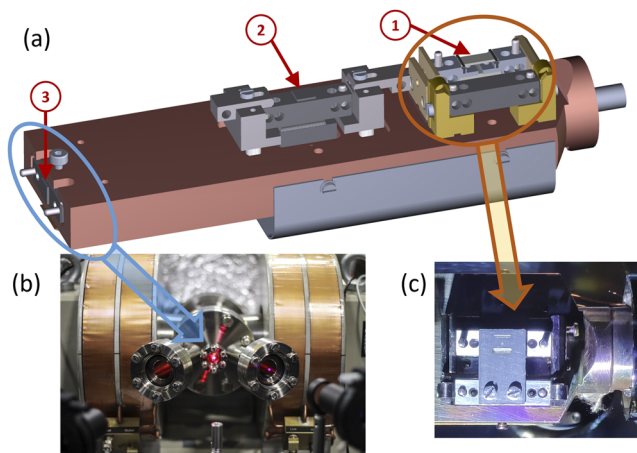


FIG. 1. Top view representation of the MBE-Cluster: MASK chamber (green), OxMBE chamber (red), XPS spectrometer chamber (blue), and the two home-built interconnection chambers (orange).



**FIG. 2.** (a) 3D representation of the MASK manipulator head. Circled numbers indicate the three sample holder locations available: (1) mask, (2) annealing, and (3) MOKE positions. (b) *In situ* MOKE measurement using a 658 nm red laser. (c) Photographic image of the mask position with an example of lithographic masks.

The samples are placed on the home-built cryogenic manipulator head, schematically represented in Fig. 2(a).

The manipulator head is made out of a block of oxygen-free high thermal conductivity (OFHC) copper; it is fixed on the head of a liquid-He flow cryostat with an indium interface to maximize thermal conductivity. The temperature is measured both at the cryostat and at the tip of the manipulator head by two silicon diode sensors, controlled via a LakeShore 335 Temperature Controller. The temperature stability at the lowest possible value is attained within 30 min, reaching 78 K with liquid nitrogen and 5 K with liquid He at the tip of the manipulator head.

Three different sample positions are available on the cryostat head [Fig. 2(a)]:

- (1) Position 1 admits up to two samples, side by side. One position is designed for hosting split sample holders with electrical contacts prepared *ex situ*, isolated from ground via a ceramic or sapphire plate. This setup allows applying a bias voltage across the sample: it was specifically designed for biasing ferroelectric substrates or multiferroic heterostructures across the 5 K–580 K range of temperature, i.e., imposing a preferential polarization state when crossing structural/ferroelectric transitions.<sup>13–15</sup>  $I(V)$  curves are measured with a picoammeter–voltage source (Keithley 6487) via BNC-UHV feedthroughs, with applied electric fields  $E$  for voltages up to 500 V.

This stage can also be used when depositing continuous or patterned metal films through lithographic masks held in the second stage, as shown in Fig. 2(c), with lateral resolution down to 100  $\mu\text{m}$ . The interchangeable masks come on dedicated sample holders.

- (2) Position 2 is a second deposition stage, which can be used either for sample growth at variable temperature or as an annealing stage. The sample heating is provided by a resistive

filament placed below the sample holder stage and shielded by a tungsten box in order to minimize irradiating the manipulator shaft and cryostat. The sample stage is electrically isolated from the manipulator head by ceramic washers. The sample can be either grounded (during film deposition) or connected to a high voltage power supply via the SHV-UHV feedthrough for sample annealing by e-bombardment, reaching temperatures up to 1000 K.

- (3) Position 3 has been specifically designed for *in situ* MOKE measurements. When the sample is placed on the tip of the manipulator head, it can be pressed by a screw against the copper block for an optimal thermal contact. The temperature is probed by a silicon diode sensor placed on the opposite side of the screw.

All electrical connections to the external feedthroughs are on the backside of the manipulator head.

*In situ* MOKE measurements are performed in a titanium square section expansion of the UHV chamber. Titanium avoids spurious hysteretic behavior coming from the UHV vessel. This section terminates with a flange hosting three quartz windows with broadband anti-reflection (BBAR) coating [Fig. 2(b)]: one looking perpendicularly to the sample surface for survey and alignment and two at a  $\pm 22^\circ$  angle from the sample normal for transmitting the external incident and reflected laser beams for MOKE measurements. The titanium square section fits in the gap of a water-cooled electromagnet (GMW 5403), controlled with a bipolar power supply (Kepko BOP 20-50MG). An in-plane  $H$  field up to  $\pm 7$  kOe [see Fig. 2(c)] can be applied uniformly to the sample volume. The rotation of the manipulator about the surface normal allows measuring longitudinal MOKE polar plots for determining the sample in-plane magnetic anisotropy. The temperature range goes from 5 K with liquid He cooling up to 580 K via local heating from the annealing stage of position 2. Magnetization curves as a function of temperature can be programmed by the temperature feedback electronics.

The MOKE setup [see Fig. 2(b)] hosts on the incident branch the linearly polarized laser [two TECBL-10GC laser sources are available, at either 405 nm (blue) or 658 nm (red) wavelength] and a Glan–Thompson polarizer. The twin laser sources allow choosing the most suitable wavelength for the sample material in order to maximize the magneto-optic response. The detection branch has a second Glan–Thompson polarizer (the analyzer) and the detector (a Thorlabs PDA25K-EC amplifier for the blue laser or a PDA100A2 for the red laser). The longitudinal MOKE can be operated either with a mechanical chopper (Thorlabs MC200B) or with a photoelastic modulator (Hinds PEM-100), connected to a lock-in amplifier (NF LI 5640).

The MOKE setup can also operate *ex situ* (in air). A vertical translation of the magnet and of the optical table supporting the laser and the two optical branches allows switching quickly between the UHV and in-air measurement configurations. In this setup, a five-axis sample holder allows measuring polar plots and carefully aligning the samples on the optical table breadboard. It includes the possibility of fixing the samples on split sample holders, thus allowing the application of an electric potential under a magnetic field for multiferroic heterostructures' characterization or magnetoresistance measurements.<sup>13</sup> A software control of all experimental parameters

and automatized metadata storage has been implemented for remote operation.

## B. OxMBE chamber: The complex oxide deposition chamber

The OxMBE chamber [whose sketch is shown in Fig. 3(a)] is devoted to the growth of nanostructured complex oxides in the form of thin films, multilayers, or superlattices. The OxMBE apparatus is optimized for the growth of complex oxide films and perovskite interfaces and for the fabrication of simple oxide-based devices. The OxMBE chamber is primarily designed for the growth of perovskites with chemical formula  $ABO_3$  in which the B-site is typically occupied by a transition-metal cation and the A-site has alkaline earth or lanthanide cations. Their growth is critically dependent upon the fine control of the atomic layering during the deposition.<sup>27</sup> Depending on the transition-metal oxidation state, bonding environment, and dimensionality, the physical properties of perovskite materials can range from

high-temperature superconductivity to ferro/antiferromagnetic behavior, ferro/piezoelectricity, and colossal magnetoresistance, among others.<sup>5,28,29</sup>

The chamber is equipped with eight effusion cells [see Fig. 3(a)], with three different setups according to the element to be deposited: three standard cells (up to 1300 °C, e.g., Mn, Co, and Fe), three high-temperature cells (up to 2000 °C, e.g., La, Cu, and Ti), and two low temperature cells (up to 700 °C, e.g., Sr, Ba, and Ca). Each cell comes with a linear pneumatic shutter, whose aperture time determines the element deposited quantity (“dose”). The typical elemental fluxes are  $\sim 1.5 \times 10^{13}$  at/cm<sup>2</sup> s, requiring  $\sim 45$  s for the deposition of one atomic layer of A- or B-site atoms for SrTiO<sub>3</sub> (STO). The chamber also includes a Reflection High-Energy Electron Diffraction (RHEED) setup (Staib 15 kV with the rocking curve option and kSpace kSA-400 software for real-time image collection and processing), an optical pyrometer (IMPAC IS 140), and a quartz crystal microbalance (QCM). This apparatus is optimized for the growth of single-crystal films and heterostructures of doped manganites/ferrites/titanites, presenting various combinations of

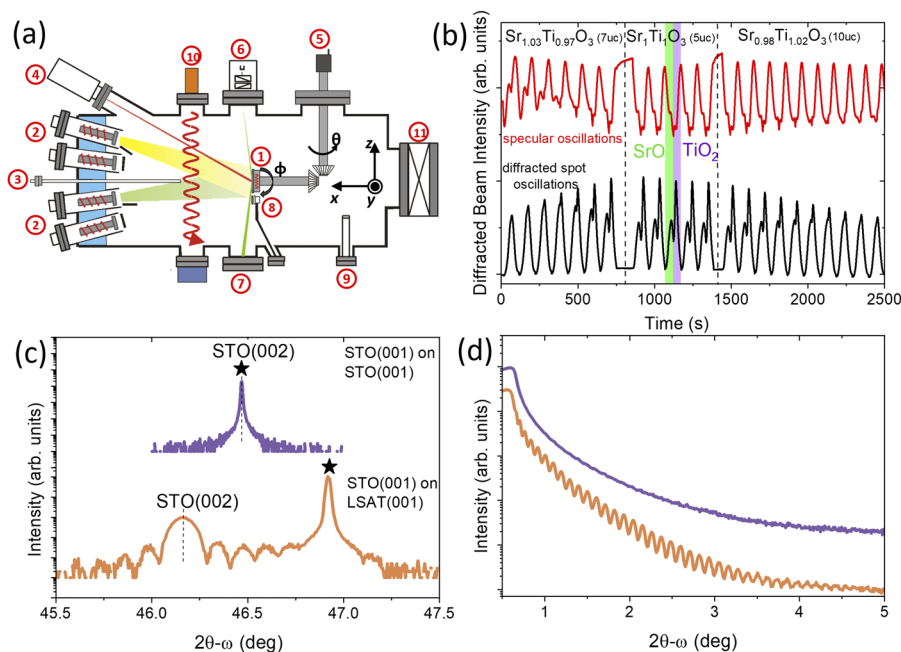


**FIG. 3.** (a) Schematic representation of the OxMBE deposition chamber. Circled numbers indicate the different components of the chamber: (1) sample, (2) Knudsen cells, (3) ozone/oxygen inlet, (4) pyrometer focused on the substrate, (5) sample manipulator with five degrees of freedom ( $x$ ,  $y$ ,  $z$ ),  $\theta$  (rotation around the  $z$ -axis), and  $\phi$  (rotation around the  $x$ -axis, i.e., substrate surface normal), (6) RHEED electron gun, (7) RHEED phosphor screen, (8) QCM, (9) mass spectrometer (RGA), (10) hollow cathode lamp for atomic absorption spectroscopy, (11) *in situ* transfer to the load lock and interconnecting chamber. (b) Stoichiometry calibration for STO growth in the alternating-shutter mode, along STO (001) and taken at a fixed incidence angle  $\sim 2.4^\circ$ , with both specular (red) and diffracted spot (black) oscillations. At time  $t = 0$ , the deposition begins on a TiO<sub>2</sub>-terminated surface. The stoichiometry of the deposited Sr and Ti can be controlled by varying the shutter times, as indicated in the plot. During the stoichiometric deposition of 5 u.c. (central region), the green-shaded area corresponds to the Sr shutter “open” time, while the purple-shaded area corresponds to the Ti shutter “open” time. Note that the total excess Sr deposited in the first 7 u.c. is compensated by the excess Ti deposited in the last 10 u.c., and the starting and ending intensities and triangular shape are identical. Repeated, cyclic oscillations of the diffracted beam, with the same shape and intensity for each cycle, are characteristic of stoichiometric growth, as discussed in the text. (c) High-resolution x-ray diffraction  $2\theta$ - $\omega$  scans around the STO(002) peak for 200 u.c. films grown on STO(001) (violet) and LSAT(001) (orange). The substrate peak is indicated by  $\star$ . Note that, for the STO film grown on the STO substrate, the film (002) peak lies under the substrate (002) peak and no finite thickness oscillations are observable, indicating that the film and substrate have identical  $c$ -axis lattice parameters. (d) X-ray reflectivity scans at a low angle for the same films in (c). For the STO film grown on the STO substrate, the absence of oscillations indicates the same electron density in both the film and substrate, and the film/substrate interface is invisible to the x rays.

ferromagnetic, antiferromagnetic, and ferroelectric properties. Molecular oxygen, pure ozone, or mixtures of the two are used to optimize the oxidizing atmosphere during growth. The combination of QCM and RHEED monitors the stoichiometry and crystal order during the growth.

OxMBE can operate either in the codeposition mode (i.e., all elements are evaporated simultaneously, with fluxes matched by adjusting cell temperatures to obtain the desired stoichiometry) or in the alternating-shutter mode (i.e., with consecutive shutter openings of different elements, with the dose defined by the shutter aperture time).<sup>27</sup> The latter method allows reproducing the natural periodic structure of perovskites, e.g., when growth occurs along the (001) direction. In codeposition growth of STO, the Sr and Ti shutters are opened simultaneously, and both specular and diffracted spot intensities oscillate sinusoidally with the period corresponding to the deposition of one complete unit cell if the fluxes are close to stoichiometric ( $\pm 5\%$ ).<sup>30</sup> This is the typical approach for the growth of perovskites by MBE. In the alternating-shutter mode [see Fig. 3(b)], the specular and diffracted intensities display forced oscillations of much larger amplitude whose distinctive form can be used to calibrate the relative and absolute A- and B-site fluxes in real time. Figure 3(b) shows the dependence of the forced oscillations on the excess A-site coverage in which alternating-shutter AO/BO<sub>2</sub> deposition is started on a TiO<sub>2</sub>-terminated surface. By intentional Sr-rich growth during the first 7 unit cells (u.c.), when more than  $\sim 0.3$  atomic layers excess A-site has accumulated on the surface, the diffracted spot intensity develops a distinctive “double peak” shape over the deposition cycle [Fig. 3(b), center]. Adjusting the shutter times to stoichiometric deposition (A:B = 1) results in a constant shape of the “double peak” oscillations. Conversely, when calibration of the shutter times yielding stoichiometric films is not known, observation of a constant shape of the diffracted beam oscillations provides the identification of correct relative A- and B-site doses (with an estimated error of  $\pm 0.2\%$  in the case of STO). As a consequence, the approach outlined here can be used for daily calibration. Confirmation of this approach for precise calibration of stoichiometry can be seen by subsequent high-resolution x-ray diffraction scans of STO films grown on STO substrates, in which the (002) film peak is indistinguishable from the substrate peak [Fig. 3(c)] and the interface does not reflect x rays at grazing incidence [Fig. 3(d)], properties not seen in heteroepitaxial films grown on (LaAlO<sub>3</sub>)<sub>0.3</sub>(Sr<sub>2</sub>TaAlO<sub>6</sub>)<sub>0.7</sub> (LSAT) (001). Applying this approach to other materials, perovskite films with the B-site occupied by Ti, Fe, and Mn can be successfully calibrated and grown with the alternating-shutter method. The resulting films typically show 2D growth and atomically flat surfaces (from the sharp RHEED patterns) and small XRD rocking curve FWHM values, all indicating high crystalline quality (see Sec. III for results on manganite films). In addition, during alternating-shutter deposition, RHEED rocking curves can be recorded at any time during the deposition cycle, allowing for a real-time analysis of the growing surface as has been done, e.g., for Si(111) growth.<sup>31</sup> Further details on the alternating-shutter calibration method using oscillations and rocking curves, and resulting film properties, will be reported in a dedicated article.

Precise control on the surface termination is essential for surface/interface engineering and can be performed *in situ* with RHEED rocking curve analysis; in combination with the MBE flexibility, it

allows successful construction of compositional sequences of perovskite heterostructures.<sup>14,32–38</sup>

### C. XPS spectrometer chamber

The XPS chamber is equipped with a 300 mm hemispherical electron energy and momentum analyzer, a water-cooled twin anode Mg/Al K<sub>α</sub> x-ray source (PSP TX400/2,  $h\nu = 1.25$  keV and 1.49 keV, respectively), and a 5-axis cryogenic sample manipulator. This part of the setup was previously developed as an end-station for bulk-sensitive photoemission on the ESRF ID16 beamline (VOLUME PhotoEmission).<sup>24–26</sup> Details on its technical specifications can be found elsewhere. It operates as a high-luminosity XPS spectrometer with energy resolution limited by the x-ray source bandwidth (1.2 eV–1.5 eV depending on the anode). Its integration in the MBE-Cluster makes it ideal for chemical surveys and core level line shape analysis as well as for preliminary characterization for those samples to be measured also with synchrotron radiation at the NFFA-APE and NFFA-SPRINT beamlines, or elsewhere.

### D. The interconnecting chambers

Compact bi-directional transfer rails and chambers, as shown in Fig. 1, have been designed and home-built at IOM-CNR. Sample carousels travel on the displaceable rails allowing for fast transport across 2.1 m of total distance, with a UHV envelope limited to only 1 m external encumbrance, reducing the total length of the apparatus. The mechanism regulating the linear transfer is shown in Fig. 4(a). Two movements can be controlled with the cranks connected to the bottom flange: one allows moving the whole rail track into the two nearby chambers, while the second one controls the movement of the carousel on the rail. The interconnecting chambers are pumped by ion pumps (Gamma Vacuum TiTan Ion Pump) and non-evaporable getter pumps (SAES-getter). Up to 12 samples can be stored and transferred under UHV conditions [see Fig. 4(b)]. Introducing and removing the samples in the cluster is assured by the load lock-fast entry chamber (see Fig. 1), equipped with a 80 l/s turbo pump (Pfeiffer HiPace 80). The load lock can transfer from air to UHV up to four sample holders in about 30 min.

A docking station for the UHV shuttle (Ferrovac VSN40S) is also available and can be installed in either of the two interconnection chambers. The UHV shuttle is pumped with a combination ion pump (SAEG NexTorr D-100-5) with an optional liquid-N<sub>2</sub> cooled trap. The interface between the cluster and the UHV shuttle is assured by a two-valve interconnect turbo pump (Agilent TwisTorr84 FS) enabling the transfer in low  $10^{-10}$  mbar pressure.

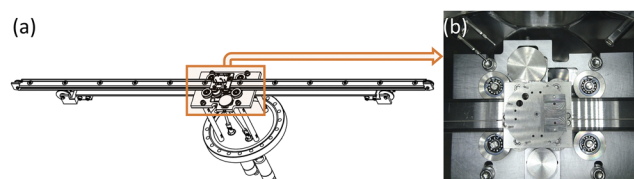


FIG. 4. (a) Sketch of the sample transfer mechanism of the transfer tube. (b) Photographic image of the central part of the transfer tube. The carousel is visible at the center, with the rail track below it.

The UHV shuttle can host up to six sample holders (three per each standard).

### III. PERFORMANCES AND APPLICATIONS

In Fig. 5, we give two examples of the high-quality, stoichiometric films achievable by the alternating-shutter method grown in the OxMBE chamber. The crystalline and transport properties of an optimally doped  $\text{La}_{1-x}\text{Sr}_x\text{MnO}_3$  (LSMO,  $x = 0.35$ ) film grown on the STO(001) substrate are presented in Figs. 5(a) and 5(b). The narrow LSMO (002) rocking curve FWHM [ $0.008^\circ$ , Fig. 5(a)] reflects the extremely high structural integrity of the film, with a crystalline coherence length longer than that of the STO substrate; this value is one of the lowest reported to date for LSMO films. As has been discussed in the literature,<sup>32</sup> the metal-insulator transition (MIT) temperature seen in the transport properties of LSMO is a sensitive measure of its stoichiometry and disorder. In contrast to Ca- and Ba-doped  $\text{LaMnO}_3$  single crystals that universally show a MIT near their Curie temperatures ( $T_{\text{Curie}}$ ), optimally doped LSMO is the only manganite phase with no MIT, remaining fully metallic up to 600 K and showing the lowest residual resistivity ( $60 \mu\Omega \text{ cm}$  at 4 K) of the manganite perovskites.<sup>39</sup> However, nearly all LSMO thin films reported in the literature show a MIT below 400 K, likely the result of off-stoichiometry (including oxygen) compared to the bulk crystals.<sup>31</sup> This contrasts the fully metallic LSMO ( $x = 0.35$ ) films [up to 500 K, inset of Fig. 5(b)] produced by OxMBE, showing a low residual resistivity ( $60 \mu\Omega \text{ cm}$ ) and high  $T_{\text{Curie}}$  (360 K) comparable with the bulk LSMO crystals.<sup>39</sup> More details on the growth and stoichiometric control of the LSMO thin films grown across the LMO-SMO phase diagram can be found in Ref. 32.

The alternating-shutter method has also been applied to grow ferroelectric BTO films, showing the values of the electric polarization close to those of bulk single crystals, with low leakage [see Figs. 5(c)–5(e)]. Epitaxial capacitor structures are grown on DyScO<sub>3</sub> (DSO) (110) substrates using a metallic LSMO film as the base electrode and polycrystalline Pt–Au as the counter-electrode. These are patterned into various lateral dimensions and wire bonded for polarization vs voltage measurements in a ferroelectric tester (Radiant Technologies, Inc., Albuquerque NM). The LSMO layer is contacted at the edge of the substrate. XRD measurements indicate that both the BTO and LSMO films are fully strained to the DSO substrates for these thicknesses, with the rocking curve FWHM similar to the DSO substrate ( $\Delta\omega < 0.01^\circ$ , not shown). This indicates the absence of threading dislocations that would be present in thicker (relaxed) BTO films and contributes to the low leakage seen in the nearly-ideal polarization loop [Fig. 5(e)].

Figures 6–8 show the representative characterizations as obtained in the MBE-Cluster. Figure 6 concerns CoFeB/MgO interfaces: The aim of this study is to grow  $\text{Co}_{60}\text{Fe}_{20}\text{B}_{20}$  by e-beam deposition in stage (2) of the manipulator of the MASK chamber [see Fig. 2(a)] at room temperature, after annealing the MgO substrate for 1 h at  $450^\circ\text{C}$  at  $p \sim 2 \times 10^{-10}$  mbar. A stoichiometric compound was deposited on atomically clean MgO [001] substrates and analyzed by XPS right after deposition. Figures 6(a) and 6(b) show the Co 2p and Fe 2p core level spectra of a 5 nm CoFeB/MgO sample, as obtained using the Mg  $K_\alpha$  source showing clean metallic lineshapes. The sample was then transferred to stage (3) for *in situ* MOKE characterization. Figure 6(c) shows the ferromagnetic hysteresis loops of a 20 nm CoFeB/MgO sample as obtained using the red laser and the mechanical chopper, rotating the sample about its surface normal in  $15^\circ$  steps. No in-plane anisotropy was observed, as expected for amorphous CoFeB and a coercive field of 25 Oe.

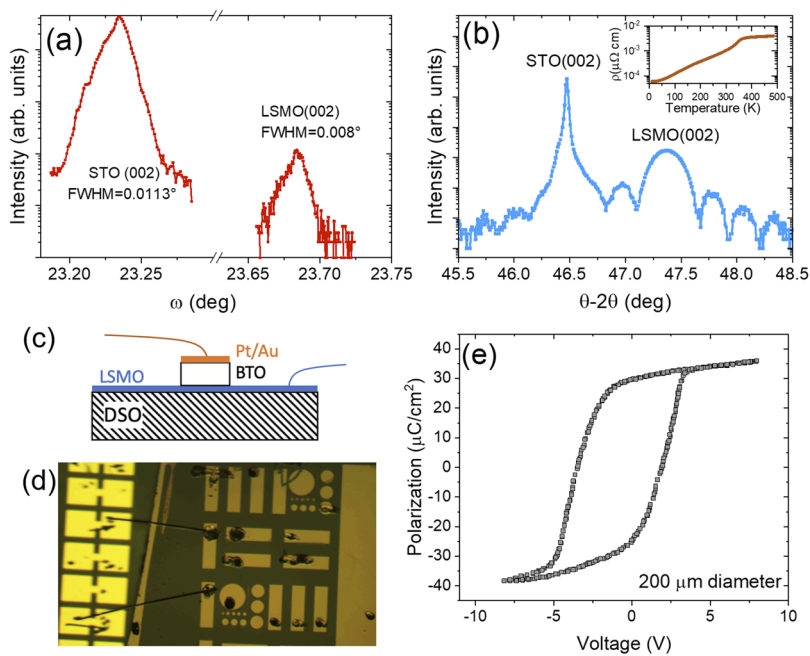


**FIG. 5.** (a) Rocking curve of STO (002) and LSMO (002) diffraction peaks for LSMO ( $x = 0.35$ ) 100 u.c. thick film grown on the STO (001) substrate. (b)  $\theta$ -2 $\theta$  XRD scan for the same film. Tensile strain leads to an out-of-plane lattice parameter for the LSMO film of 3.83 Å. (Inset) Resistivity vs temperature for an LSMO ( $x = 0.35$ ) film showing metallic behavior up to 500 K and  $T_{\text{Curie}} = 360$  K. (c) Schematic of the capacitor structure to measure the ferroelectric properties of BTO films. Epitaxial films of LSMO and BTO are grown on the DSO(110) substrate and capped by a Pt/Au electrode. (d) The heterostructure is patterned into various shapes from  $10 \mu\text{m}^2$  circles to  $400 \times 100 \mu\text{m}^2$  rectangles, as seen in the optical image of a wire bonded sample. (e) An example of a polarization vs voltage hysteresis loop for an 80 nm BTO film taken at room temperature with 2 ms period. The saturation polarization of  $\sim 30 \mu\text{C}/\text{cm}^2$  is comparable with bulk BTO crystals and high-quality BTO films.

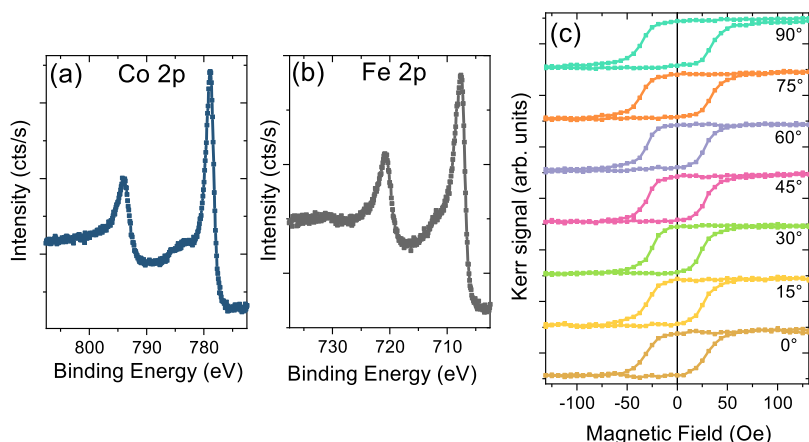


**FIG. 6.** (a) Co 2p and (b) Fe 2p edges of a CoFeB (5 nm)/MgO sample after deposition in the MASK chamber. The spectra were taken with the Mg source. (c) Rotational MOKE characterization at room temperature of a CoFeB (20 nm)/MgO [001] sample deposited in the MASK chamber. The hysteresis loops have been measured at room temperature, rotating the sample in plane every 15°.

Figure 7 shows the data obtained from a LSMO ( $x = 0.35$ ) 100 u.c. film epitaxially grown in the OxMBE chamber on the LSAT [001] substrate in an oxygen pressure of  $2 \times 10^{-7}$  mbar and with RHEED assisted *in operando* analysis. Figure 7(a) presents the RHEED pattern of the 100 u.c. thick LSMO film. Elevated half-order diffraction spots (circled in white) are associated with the orthorhombic structure of the deposited LSMO, which are not present for the cubic substrate. Once transferred to the MASK chamber, the sample was analyzed by *in situ* MOKE at 77 K. The results of the rotational MOKE measurements [see Figs. 7(b)–7(d)] show a clear uniaxial anisotropy along the (010) direction, with a hard axis along the (100) plane, consistent with that reported in the literature.<sup>40</sup> These measurements were obtained using the blue laser, since, at 405 nm wavelength (3.06 eV), the Kerr rotation is optimal for LSMO thin films.<sup>41,42</sup>

Figure 8 shows some examples of sample characterizations performed in the MASK chamber: Fig. 8(a) shows the MOKE for an exchange biased sample, with stack Pt(2)/Co(5)/IrMn(3)/Pt(7.2)/a(3) (in parentheses are reported the layer thicknesses in nm), deposited on a Si wafer. The magnetic field was applied along the easy axis of the exchange bias, which was previously set with a field cooling procedure at an annealing temperature of 580 K and under a magnetic field of +2 kOe at Spintec.<sup>43</sup> The hysteresis loop of the sample after this exchange bias setting is shown in green. Subsequently, the sample temperature was raised in the *in situ* MOKE position up to 580 K and then cooled down to 300 K under a setting field of -2 kOe. This operation was done to reverse the sign of the interfacial exchange bias field. The same annealing temperature and setting field (with opposite sign) are expected to give a symmetric hysteresis loop compared to the starting one.<sup>44,45</sup> Indeed, the obtained

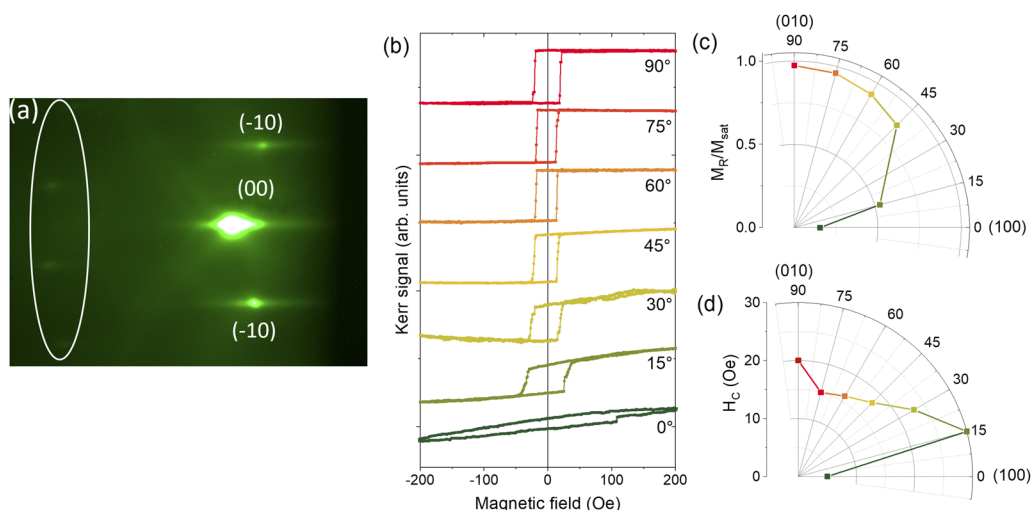


**FIG. 7.** (a) RHEED pattern of a 100 u.c. thick LSMO ( $x = 0.35$ ) film deposited on LSAT [001]. Inside the circle, the half-order spots can be seen; [(b)–(d)] rotational MOKE characterization at 77 K of a LSMO (100 u.c.)/LSAT [001] sample deposited in the OxMBE chamber, with (b) the measured hysteresis loops for a selection of in-plane angles and the corresponding polar plots for (c) magnetization remanence  $M_R/M_{sat}$  and (d) coercive field  $H_c$ .

16 November 2024 16:36:54



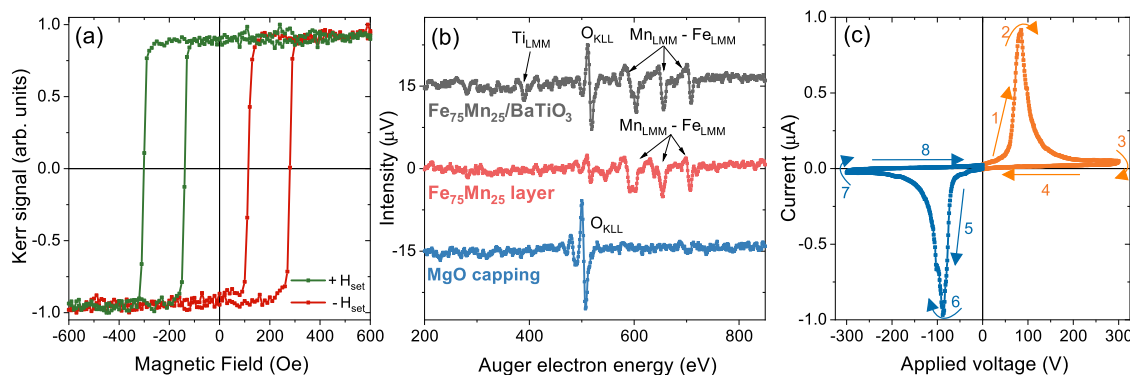


**FIG. 8.** (a) *In situ* MOKE measurements on a Co (5 nm)/IrMn (3 nm) sample after annealing and field cooling under either a +2 kOe setting field (green) or a −2 kOe setting field (red). (b) AES measurements of a  $\text{Fe}_{75}\text{Mn}_{25}/\text{BaTiO}_3$  sample during the different deposition steps. (c)  $I(V)$  curve of the Fe (3 nm)/PMN-PT sample with the substrate ferroelectric switching around  $\pm 100$  V. The arrows are guides for following the switching of the voltage, starting with a positive bias and followed by a negative bias.

hysteresis loop, measured at room temperature, evolved to the one shown in Fig. 8(a) in red. The exchange bias direction was effectively reversed, maintaining similar values of exchange bias and coercivity as in the previous setting.

Figure 8(b) shows the AES spectra measured in-between the growth of the different layers of a 6 nm thick  $\text{Fe}_{75}\text{Mn}_{25}$  sample on a 200 u.c.  $\text{BaTiO}_3$  thin film on the  $\text{SrTiO}_3$  [001] substrate. After deposition of the  $\text{BaTiO}_3$  thin film layer in the OxMBE chamber, the sample was transferred to the MASK chamber. Here, a first sub-nm calibrated co-deposition of Fe and Mn was done,<sup>15</sup> followed by AES analysis of the  $\text{Fe}_{75}\text{Mn}_{25}/\text{BaTiO}_3$  interface [gray curve in Fig. 8(b)]. After a second *in situ* deposition step of  $\text{Fe}_{75}\text{Mn}_{25}$  up to its final thickness, the Auger spectra (red curve) did not show  $\text{O}_{\text{KLL}}$  and  $\text{Ti}_{\text{LMM}}$  peaks (at 510 eV–515 eV and 370 eV–400 eV energies, respectively) anymore, but only those of  $\text{Fe}_{\text{LMM}}$  and  $\text{Mn}_{\text{LMM}}$  (between 600 eV and 750 eV). After that, a capping layer of 2 nm of MgO was deposited by electron bombardment of a MgO single crystal. The resulting Auger spectrum (blue curve) shows the clear  $\text{O}_{\text{KLL}}$  peak, while no Fe or Mn peaks are detected, indicating that the MgO capping layer has a thickness larger than the probing depth of the Auger measurement ( $\sim 1$  nm), as expected by design.

Finally, Fig. 8(c) shows an example of the  $I(V)$  curve measured on a Fe (3 nm)/PMN-PT sample while switching the polarization of the substrate.<sup>15</sup> The Fe layer was deposited in the MASK chamber with a protective capping layer of 2 nm MgO on top of it, on a pristine PMN-PT substrate. After deposition, electrical contacts were prepared *ex situ* on split sample holders using silver paste as the backside electrode and a gold wire as the top contact. The peaks in the current intensity correspond to the ferroelectric switching of the substrate.

#### IV. CONCLUSIONS

The present paper describes the design and specifications of the MBE-Cluster ensemble and representative examples of studies performed *in situ* with the setup. The extra feature of easy UHV exchange of the samples with the nearby NFFA-APE beamlines (XAS/XMCD and Spin-ARPES) at Sincrotrone-Trieste and

NFFA-SPRINT laser-HHG beamline for time-resolved spectroscopy and magnetometry makes it possible to perform nanoscience studies from the sample synthesis to the ultimate fine structure analysis.

Thanks to its versatility, the MBE-Cluster is a core part of the NFFA users facility with access through the NFFA Research Infrastructure programs.<sup>22,23</sup>

#### ACKNOWLEDGMENTS

This work was performed in the framework of the Nanoscience Foundry and Fine Analysis (NFFA-MIUR Italy Progetti Internazionali) project. This article is *in memoriam* of our colleagues Roberta Ciprian and Aleksander Deluisa who strongly contributed to the design and development of the apparatus.

#### DATA AVAILABILITY

The data that support the findings of this study are available from the corresponding author upon reasonable request.

#### REFERENCES

- <sup>1</sup>S. Franchi, in *Molecular Beam Epitaxy*, edited by M. Henini (Elsevier, Oxford, 2013), pp. 1–46.
- <sup>2</sup>W. P. McCray, *Nat. Nanotechnol.* **2**, 259 (2007).
- <sup>3</sup>H. Y. Hwang, Y. Iwasa, M. Kawasaki, B. Keimer, N. Nagaosa, and Y. Tokura, *Nat. Mater.* **11**, 103 (2012).
- <sup>4</sup>F. Hellman, M. S. Division, L. Berkeley, A. Hoffmann, G. S. D. Beach, E. E. Fullerton, A. H. Macdonald, and D. C. Ralph, *Rev. Mod. Phys.* **89**, 025006 (2017).
- <sup>5</sup>P. Zubko, S. Gariglio, M. Gabay, P. Ghosez, and J.-M. Triscone, *Annu. Rev. Condens. Matter Phys.* **2**, 141 (2011).
- <sup>6</sup>M. Bibes, J. E. Villegas, and A. Barthélémy, *Adv. Phys.* **60**, 5 (2011).
- <sup>7</sup>H. Béa, M. Gajek, M. Bibes, and A. Barthélémy, *J. Phys.: Condens. Matter* **20**, 434221 (2008).
- <sup>8</sup>S. Manipatruni, D. E. Nikonov, C.-C. Lin, T. A. Gosavi, H. Liu, B. Prasad, Y.-L. Huang, E. Bonturim, R. Ramesh, and I. A. Young, *Nature* **565**, 35 (2019).
- <sup>9</sup>S. Fusil, V. Garcia, A. Barthélémy, and M. Bibes, *Annu. Rev. Mater. Res.* **44**, 91 (2014).

- <sup>10</sup>P. B. Meisenheimer, S. Novakov, N. M. Vu, and J. T. Heron, *J. Appl. Phys.* **123**, 240901 (2018).
- <sup>11</sup>T. Jungwirth, X. Marti, P. Wadley, and J. Wunderlich, *Nat. Nanotechnol.* **11**, 231 (2016).
- <sup>12</sup>Z. Feng, H. Yan, and Z. Liu, *Adv. Electron. Mater.* **5**, 1800466 (2019).
- <sup>13</sup>G. Vinai, B. Ressel, P. Torelli, F. Loi, B. Gobaut, R. Ciancio, B. Casarin, A. Caretta, L. Capasso, F. Parmigiani, F. Cugini, M. Solzi, M. Malvestuto, and R. Ciprian, *Nanoscale* **10**, 1326 (2018).
- <sup>14</sup>F. Motti, G. Vinai, A. Petrov, B. A. Davidson, B. Gobaut, A. Filippetti, G. Rossi, G. Panaccione, and P. Torelli, *Phys. Rev. B* **97**, 094423 (2018).
- <sup>15</sup>G. Vinai, F. Motti, V. Bonanni, A. Y. Petrov, S. Benedetti, C. Rinaldi, M. Stella, D. Cassese, S. Prato, M. Cantoni, G. Rossi, G. Panaccione, and P. Torelli, *Adv. Electron. Mater.* **5**, 1900150 (2019).
- <sup>16</sup>S. K. Chaluvadi, F. Ajejas, P. Orgiani, O. Rousseau, G. Vinai, A. Y. Petrov, P. Torelli, A. Pautrat, J. Camarero, P. Perna, and L. Mechin, *Appl. Phys. Lett.* **113**, 052403 (2018).
- <sup>17</sup>G. Panaccione, I. Vobornik, J. Fujii, D. Krizmancic, E. Annese, L. Giovanelli, F. Maccherozzi, F. Salvador, A. De Luisa, D. Benedetti, A. Gruden, P. Bertoch, F. Polack, D. Cocco, G. Sostero, B. Diviacco, M. Hochstrasser, U. Maier, D. Pescia, C. H. Back, T. Greber, J. Osterwalder, M. Galaktionov, M. Sancrotti, and G. Rossi, *Rev. Sci. Instrum.* **80**, 043105 (2009).
- <sup>18</sup>M.-A. Husanu and C. A. F. Vaz, *Spectroscopy of Complex Oxide Interfaces* (Springer International Publishing, 2018), pp. 245–281.
- <sup>19</sup>T. Pincelli, V. N. Petrov, G. Brajnik, R. Ciprian, V. Lollobrigida, P. Torelli, D. Krizmancic, F. Salvador, A. De Luisa, R. Sergio, A. Gubertini, G. Cautero, S. Carrato, G. Rossi, and G. Panaccione, *Rev. Sci. Instrum.* **87**, 035111 (2016).
- <sup>20</sup>R. Cucini, T. Pincelli, G. Panaccione, D. Kopic, F. Frassetto, G. M. Pierantozzi, S. Peli, A. Fondacaro, A. De Luisa, D. Vita, P. Carrara, D. Krizmancic, D. T. Payne, F. Salvador, A. Sterzi, F. Parmigiani, G. Rossi, F. Cilento, A. Fondacaro, A. De Luisa, and A. De Vita, *Struct. Dyn.* **7**, 014303 (2020).
- <sup>21</sup>R. Bertacco, M. Cantoni, M. Riva, A. Tagliaferri, and F. Ciccacci, *Appl. Surf. Sci.* **252**, 1754 (2005).
- <sup>22</sup>Open access is performed via the website, <https://trieste.nffa.eu/>, 2015.
- <sup>23</sup>See <https://www.nffa.eu/> for details on the platform and its offer.
- <sup>24</sup>P. Torelli, M. Sacchi, G. Cautero, M. Cautero, B. Krastanov, P. Lacovig, P. Pittana, R. Sergio, R. Tommasini, A. Fondacaro, F. Offi, G. Paolicelli, G. Stefani, M. Grioni, R. Verbeni, G. Monaco, and G. Panaccione, *Rev. Sci. Instrum.* **76**, 023909 (2005).
- <sup>25</sup>G. Panaccione, G. Cautero, A. Fondacaro, M. Grioni, P. Lacovig, G. Monaco, F. Offi, G. Paolicelli, M. Sacchi, G. Stefani, and P. Torelli, *Nucl. Instrum. Methods Phys. Res., Sect. A* **547**, 56 (2005).
- <sup>26</sup>G. Panaccione, F. Offi, M. Sacchi, and P. Torelli, *C. R. Phys.* **9**, 524 (2008).
- <sup>27</sup>D. G. Schlom, L.-Q. Chen, X. Pan, A. Schmehl, and M. A. Zurbuchen, *J. Am. Ceram. Soc.* **91**, 2429 (2008).
- <sup>28</sup>C. A. F. Vaz, J. Hoffman, C. H. Ahn, and R. Ramesh, *Adv. Mater.* **22**, 2900 (2010).
- <sup>29</sup>J. L. MacManus-Driscoll, M. P. Wells, C. Yun, J.-W. Lee, C.-B. Eom, and D. G. Schlom, *APL Mater.* **8**, 040904 (2020).
- <sup>30</sup>A. Ichimiya and P. I. Cohen, *Reflection High-Energy Electron Diffraction* (Cambridge University Press, 2004).
- <sup>31</sup>R. Bertacco, A. Tagliaferri, M. Riva, L. Signorini, M. Cantoni, A. Cattoni, F. Ciccacci, B. A. Davidson, F. Maccherozzi, I. Vobornik, and G. Panaccione, *Phys. Rev. B* **78**, 035448 (2008).
- <sup>32</sup>A. Y. Petrov, X. Torrelles, A. Verna, H. Xu, A. Cossaro, M. Pedio, J. Garcia-Barriocanal, G. R. Castro, and B. A. Davidson, *Adv. Mater.* **25**, 4043 (2013).
- <sup>33</sup>T. Pincelli, V. Lollobrigida, F. Borgatti, A. Regoutz, B. Gobaut, C. Schlueter, T.-L. Lee, D. J. J. Payne, M. Oura, K. Tamasaku, A. Y. Petrov, P. Graziosi, F. Miletto Granozio, M. Cavallini, G. Vinai, R. Ciprian, C. H. Back, G. Rossi, M. Taguchi, H. Daimon, G. Van Der Laan, and G. Panaccione, *Nat. Commun.* **8**, 16041 (2017).
- <sup>34</sup>T. Pincelli, R. Cucini, A. Verna, F. Borgatti, M. Oura, K. Tamasaku, H. Osawa, T.-L. Lee, C. Schlueter, S. Günther, C. H. Back, M. Dell'Angela, R. Ciprian, P. Orgiani, A. Petrov, F. Sirotti, V. A. Dediu, I. Bergenti, P. Graziosi, F. Miletto Granozio, Y. Tanaka, M. Taguchi, H. Daimon, J. Fujii, G. Rossi, and G. Panaccione, *Phys. Rev. B* **100**, 045118 (2019).
- <sup>35</sup>C. Schlueter, P. Orgiani, T. L. Lee, A. Y. Petrov, A. Galdi, B. A. Davidson, J. Zegenhagen, and C. Aruta, *Phys. Rev. B* **86**, 155102 (2012).
- <sup>36</sup>C. Aruta, M. Minola, A. Galdi, R. Ciancio, A. Y. Petrov, N. B. Brookes, G. Ghiringhelli, L. Maritato, and P. Orgiani, *Phys. Rev. B* **86**, 115132 (2012).
- <sup>37</sup>A. Verna, B. A. Davidson, Y. Szeto, A. Y. Petrov, A. Mirone, A. Giglia, N. Mahne, and S. Nannarone, *J. Magn. Magn. Mater.* **322**, 1212 (2010).
- <sup>38</sup>P. Orgiani, A. Y. Petrov, R. Ciancio, A. Galdi, L. Maritato, and B. A. Davidson, *Appl. Phys. Lett.* **100**, 042404 (2012).
- <sup>39</sup>A. Urushibara, Y. Moritomo, T. Arima, A. Asamitsu, G. Kido, and Y. Tokura, *Phys. Rev. B* **51**, 14103 (1995).
- <sup>40</sup>H. Boschker, M. Mathews, P. Brinks, E. Houwman, A. Vailionis, G. Koster, D. H. A. Blank, and G. Rijnders, *J. Magn. Magn. Mater.* **323**, 2632 (2011).
- <sup>41</sup>S. Yamaguchi, Y. Okimoto, K. Ishibashi, and Y. Tokura, *Phys. Rev. B* **58**, 6862 (1998).
- <sup>42</sup>M. Veis, Š. Višňovský, P. Lecoeur, A.-M. Haghiri-Gosnet, J.-P. Renard, P. Beauvillain, W. Prellier, B. Mercey, J. Mistrík, and T. Yamaguchi, *J. Phys. D: Appl. Phys.* **42**, 195002 (2009).
- <sup>43</sup>G. Vinai, L. Frangou, C. Castan-Guerrero, V. Bonanni, B. Gobaut, S. Auffret, I. L. Prejbeanu, B. Dieny, V. Baltz, and P. Torelli, *J. Phys.: Conf. Ser.* **903**, 012061 (2017).
- <sup>44</sup>K. O'Grady, L. E. Fernandez-Outon, and G. Vallejo-Fernandez, *J. Magn. Magn. Mater.* **322**, 883 (2009).
- <sup>45</sup>G. Vinai, J. Moritz, S. Bandiera, I. L. Prejbeanu, and B. Dieny, *J. Phys. D: Appl. Phys.* **46**, 322001 (2013).